

# Superconductivity enhancement and doping-dependent phase diagram of Sm-based oxypnictides by high-pressure growth technique

Mohammad Azam<sup>1</sup>, Tatiana Zajarniuk<sup>2</sup>, Ryszard Didusko<sup>2,3</sup>, Taras Palasyuk<sup>4</sup>, Cezariusz Jastrzebski<sup>4</sup>, Andrzej Szewczyk<sup>2</sup>, Hiraku Ogino<sup>5</sup>, Shiv J. Singh<sup>1\*</sup>

<sup>1</sup>*Institute of High Pressure Physics (IHPP), Polish Academy of Sciences, Sokołowska 29/37, 01-142 Warsaw, Poland*

<sup>2</sup>*Institute of Physics, Polish Academy of Sciences, Aleja Lotników 32/46, 02-668 Warsaw, Poland*

<sup>3</sup>*National Centre for Nuclear Research, ul. Andrzeja Sołtana 7/3, 05-400 Otwock-Swierk, Poland*

<sup>4</sup>*Faculty of Physics, Warsaw University of Technology, Koszykowa 75, 00-662 Warsaw, Poland*

<sup>5</sup>*Core Electronics Technology Research Institute, National Institute of Advanced Industrial Science and Technology (AIST), Tsukuba, Ibaraki 305-8568, Japan*

**\*Corresponding author:**

Email: [sjs@unipress.waw.pl](mailto:sjs@unipress.waw.pl)

<https://orcid.org/0000-0001-5769-1787>

## Abstract

A series of  $\text{SmFeAsO}_{1-x}\text{F}_x$  (Sm1111) bulk samples ( $0.05 \leq x \leq 0.40$ ) are synthesized using an *in-situ* cubic-anvil high-pressure (CA-HP) technique at 4 GPa and are characterized through structural, microstructural, Raman, transport, and magnetic measurements. A systematic reduction of lattice parameters and unit-cell volume confirms effective fluorine substitution at oxygen sites, while Raman spectroscopy reveals electron doping and subtle changes in local bonding environments. In the underdoped regime ( $0.05 \leq x < 0.2$ ), the superconducting transition temperature ( $T_c$ ) is enhanced by 10-17 K and the critical current density ( $J_c$ ) is increased by up to an order of magnitude. The upper critical field ( $H_{c2}$ ), estimated using the Werthamer–Helfand–Hohenberg model, reaches  $\sim 200$  T, indicating strong spin paramagnetic effects and multiband superconductivity. Resistive broadening under applied fields follows Arrhenius behavior, with the activation energy showing a power-law field dependence that decreases rapidly at higher fields, consistent with collective vortex pinning. The superconducting phase diagram constructed from  $T_c$  and  $J_c$  versus fluorine content reveals a dome-like trend, with a maximum  $T_c$  of 57 K and  $J_c$  of  $10^4 \text{ A cm}^{-2}$  at the optimal doped region. A direct comparison with CSP samples demonstrates that high-pressure synthesis simultaneously enhances both  $T_c$  and  $J_c$  across the entire fluorine-doping range. These findings establish high-pressure growth as a highly effective approach for optimizing iron-based superconductors and underscore its potential for both fundamental research and future high-field applications.

## Keywords

Iron-based superconductors; 1111 oxypnictide; cubic-anvil high-pressure synthesis; upper critical field; critical current density

## Introduction:

The discovery of iron-based superconductors (FBS), particularly the layered oxypnictide  $REFeAsO$  ( $RE$  = rare earth; 1111) systems [1], has significantly advanced the field of high-temperature superconductivity [2, 3, 4]. Among these, fluorine-doped  $SmFeAsO_{1-x}F_x$  (Sm1111) exhibits the highest superconducting transition temperature ( $T_c \approx 57$ -58 K) reported for FBS [5, 6, 7, 8], along with exceptionally high upper critical fields ( $\mu_0 H_{c2} \approx 200$ -300 T) [6, 9]. These properties make Sm1111 a promising candidate for high-magnetic-field applications without the need for liquid helium cooling [6, 10, 11]. Despite the few studies based on the growth of F-doped Sm1111 single crystals with critical current densities ( $J_c$ ) of  $\sim 10^6$  A/cm<sup>2</sup> at low temperatures [12], synthesizing high-quality bulk and single-crystalline samples remains challenging [10]. Structurally, the 1111-type compounds comprise electronically active FeAs layers, which host superconductivity, alternated with  $REO$  charge-reservoir layers [13]. The parent  $REFeAsO$  compound is non-superconducting and undergoes an antiferromagnetic spin-density-wave (SDW) transition near 150 K [5]. Superconductivity emerges upon carrier doping that suppresses this SDW order [14]. In  $SmFeAsO$ , electron doping via partial substitution of  $O^{2-}$  by  $F^-$  in the  $SmO$  layer [15] transfers charge carriers into the Fe 3d bands, forming quasi-two-dimensional Fermi surfaces consisting of hole pockets at the  $\Gamma$  point and electron pockets at the M point [13]. Nesting between these pockets enhances interband scattering and promotes spin fluctuations, consistent with an  $s\pm$  pairing symmetry mediated by spin fluctuations [16, 17] [18, 19]. Fluorine doping also tunes the local structure of the FeAs layers. Two geometric parameters, the As-Fe-As bond angle (ideal  $\approx 109.5^\circ$ ) and the pnictogen height ( $h_{As}$ ) above the Fe plane, correlate strongly with superconducting pairing strength [14] [20] [7]. Approaching the ideal tetrahedral geometry and optimizing  $h_{As}$  are believed to enhance the density of states and spin-fluctuation spectrum, thereby favoring higher  $T_c$  [21] [22]. Achieving this structural optimization experimentally, however, is highly nontrivial.

Conventional synthesis process at ambient pressure (CSP) is limited by fluorine volatility, unstable oxygen activity, and competition from secondary phases such as  $SmOF/Sm_2O_3$ ,  $SmAs$ , and  $FeAs$ . These factors limit fluorine solubility, degrade phase purity, and reduce sample density and intergranular connectivity, leading to low  $J_c$  values [4] [10]. Low-temperature CSP has improved fluorine retention and achieved  $T_c$  values close to 58 K, suggesting that higher F content can be stabilized when volatility and parasitic reactions are minimized. Nevertheless, the corresponding  $J_c$  remains on the order of  $10^3$  A/cm<sup>2</sup> at 5 K [6]. In

contrast, high-temperature CSP ( $\sim 1200^\circ\text{C}$ ) improves  $J_c$  by about one order of magnitude but reduces  $T_c$  by  $\sim 4$  K due to enhanced fluorine evaporation [23]. Thus, achieving both high  $T_c$  and high  $J_c$  simultaneously via CSP remains difficult.

To overcome these limitations, high-pressure (HP) synthesis has emerged as a powerful alternative. HP techniques significantly improve sample density, phase purity, and compositional homogeneity, thereby enhancing superconducting performance [24] [25, 26]. For instance, Ren et al. synthesized  $\text{SmFeAsO}_{0.90}\text{F}_{0.10}$  with  $T_c \approx 55$  K [27] and  $\text{NdFeAsO}_{0.89}\text{F}_{0.10}$  [28] with  $T_c = 51.9$  K under 6 GPa [23]. Oxygen-deficient  $\text{REFeAsO}_{1-x}$  phases have also been stabilized exclusively under high pressure [19,24] [29]. More recently, improvements in superconductivity through HP methods have been reported for  $\text{FeSe}_{0.5}\text{Te}_{0.5}$  [25],  $\text{CaKFe}_4\text{As}_4$  [26], and F-doped  $\text{SmFeAsO}$  [30, 31]. Spark plasma sintering (SPS) has also yielded denser and cleaner  $\text{Sm1111}$  samples near optimal doping ( $x \approx 0.20$ ) [32]. Despite these advances, most HP and SPS studies remain confined to compositions near optimal doping ( $\sim 20\%$  F), leaving the underdoped and, especially, overdoped regimes ( $x > 0.25$ ) largely unexplored, primarily due to the volatility of fluorine under ambient conditions. A systematic investigation across a wider doping range is essential to fully establish the superconducting phase diagram and optimize both  $T_c$  and  $J_c$  for applications.

In this work, we have presented a comprehensive study of  $\text{SmFeAsO}_{1-x}\text{F}_x$  ( $0.05 \leq x \leq 0.40$ ) polycrystalline samples synthesized under 4 GPa using a cubic-anvil high-pressure (CA-HP) technique. Maintaining identical synthesis conditions allowed us to systematically examine the influence of fluorine doping on structural parameters, phase formation, and superconducting properties, including the transition temperature ( $T_c$ ), the upper critical field ( $H_{c2}$ ), critical current density ( $J_c$ ), residual resistivity ratio ( $RRR$ ), activation energy, and phase composition. Comparative analysis with earlier reports based on conventionally synthesized samples provides new insights into the evolution of structure and superconductivity across the underdoped to overdoped regimes. The results demonstrate the effectiveness of high-pressure synthesis in producing dense, homogeneous  $\text{Sm1111}$  samples with enhanced superconducting performance.

## Experimental details:

$\text{SmFeAsO}_{1-x}\text{F}_x$  bulks were prepared using a single-step *in-situ* method under cubic-anvil high-pressure (CA-HP) technique. To ensure phase purity and compositional uniformity, the

high-purity precursors were employed, including samarium (Sm, 99.9%), iron (Fe, 99.99%), arsenic (As, 99.99%), iron (III) oxide ( $\text{Fe}_2\text{O}_3$ , 99%), and iron (II) fluoride ( $\text{FeF}_2$ , 99%). Due to the high volatility and reactivity of elemental arsenic, a preliminary synthesis of SmAs was conducted. Stoichiometric proportions of Sm and As were finely ground, compacted into pellets, which were then enclosed within a tantalum tube. This tube was then sealed in an evacuated quartz ampoule, which was heated at 550 °C for 15 hours, resulting in the formation of the SmAs phase. The resulting SmAs was then mixed with Fe,  $\text{Fe}_2\text{O}_3$ , and  $\text{FeF}_2$  according to the stoichiometric chemical formula of  $\text{SmFeAsO}_{1-x}\text{F}_x$ . For each fluorine doping content, approximately 0.45 grams of the mixed powder was prepared. These mixtures were pressed into disc-shaped pellets (diameter~6 mm) under a uniaxial pressure of 200 bar. The compacted pellets were placed into a boron nitride (BN) crucible. This crucible was placed within a pyrophyllite-based pressure medium to ensure efficient and uniform transmission of the high pressure to the sample during the synthesis process [33, 30]. A graphite tube served as the heating element in the high-pressure assembly. All in-situ CA-HP synthesis experiments were performed under identical conditions at 1400 °C and 4 GPa for 1 h. After the reaction, the samples were cooled to room temperature under pressure and subsequently characterized using structural, microstructural, and superconducting property measurements. In this study, we have defined three fluorine doping levels: underdoped region  $0.05 \leq x < 0.2$ ; optimal doped region  $0.2 \leq x \leq 0.25$ ; and overdoped region  $0.25 < x \leq 0.4$ .

X-ray diffraction (XRD) measurements were performed using a Rigaku SmartLab 3 kW diffractometer equipped with filtered  $\text{Cu-K}_\alpha$  radiation ( $\lambda = 1.5418 \text{ \AA}$ ), operating at 30 mA and 40 kV. Data were recorded over a  $2\theta$  range of 20°-70° with a step size of 0.02°/min using a Dtex250 linear detector. Lattice parameters were refined using BRUKER'S DIFFRAC.TOPAS software in conjunction with the ICDD PDF5+ 2024 database. Microstructural observations were conducted using an ultra-high-resolution nano-scanning electron microscope (nano-SEM). Magnetic characterizations were performed using a vibrating sample magnetometer (VSM) integrated into a Physical Property Measurement System (PPMS). The magnetic susceptibility was measured under a constant magnetic field of 20 Oe across a temperature range of 5-60 K. Magnetisation hysteresis ( $M$ - $H$ ) measurements were also conducted at 5 K under the external magnetic fields of up to 9 T. The temperature-dependent electrical resistivity was measured using the standard four-probe technique within the PPMS under the applied magnetic fields up to 9 T. Raman spectroscopy was performed using a Horiba Jobin Yvon LabRam ARAMIS spectrometer. The excitation source was a He-Ne ion laser emitting the

visible light at the wavelength of 632.8 nm. The laser beam was focused to achieve a spot size of less than 3 mm on the specimen surface using a 100× objective lens (numerical aperture = 0.95), which also collected the backscattered radiation. A charge-coupled device (CCD) detector was used to detect the scattered light, which was dispersed by a diffraction grating of 2400 lines/mm. Stokes spectra were recorded within the 95-300 cm<sup>-1</sup> range with an acquisition time of 300 s for each spectrum. The laser power was reduced to approximately 140 μW to avoid local heating effects in the sample.

## Results:

Powder XRD patterns of SmFeAsO<sub>1-x</sub>F<sub>x</sub> (0.05 ≤ *x* ≤ 0.40) bulks synthesized under high pressure are shown in Figure 1(a), confirming the formation of the tetragonal ZrCuSiAs-type structure (space group: *P4/nmm*) across the full composition range, consistent with previous reports [34]. In addition to the main SmFeAsO<sub>1-x</sub>F<sub>x</sub> reflections, weak impurity peaks corresponding to SmOF, SmAs, and FeAs phases are observed, which become more pronounced at higher fluorine concentrations (*x* ≥ 0.25). In the underdoped region (*x* < 0.2), small amounts of secondary phases, including SmOF and SmAs, are detected. For the optimal doped sample i.e., *x* = 0.2, the SmOF content is slightly increased compared to underdoped samples, while SmAs is nearly absent. However, for fluorine contents above 20% i.e., *x* > 0.2, the impurity phases SmOF and SmAs are increased rapidly, and a new FeAs phase is also detected, indicating that over-doping with fluorine contents promotes the formation of SmOF and segregation of SmAs/FeAs. A similar trend has been reported for CSP-synthesized SmFeAsO<sub>1-x</sub>F<sub>x</sub>, where lightly doped samples are nearly single phase, but *x* = 0.25 contains significant impurities [6]. Notably, in the present study, we successfully achieved fluorine doping up to 40% while retaining the tetragonal superconducting phase as the dominant phase. To the best of our knowledge, this is the first report of synthesizing Sm1111 with up to 40% fluorine doping using a high-pressure growth method.

A magnified view of the main (102) reflection of the tetragonal superconducting phase is shown in Figure 1(b), revealing a systematic shift of the peak position toward higher 2θ with increasing fluorine content. This provides clear evidence of reduced interplanar spacing and lattice contraction due to fluorine substitution at the oxygen site. The lattice parameters *a* and *c*, and the unit-cell volume *V* were determined by least-squares refinements and are presented in Figures 1(c)-1(e). For comparison, the reported lattice parameters for F-doped Sm1111

prepared via the CSP method are also included [6] in these figures. The *in-plane* lattice parameter  $a$  decrease steadily from 3.928(1) Å at  $x = 0.05$  to 3.912(1) Å at  $x = 0.30$  and remains nearly constant at 3.913(1) Å for  $x = 0.40$  (Figure 1(c)). In contrast, the *out-of-plane* lattice parameter  $c$  exhibits a weakly non-monotonic decrease from 8.468(1) Å at  $x = 0.05$  to 8.455(3) Å at  $x = 0.30$ , remaining nearly unchanged at  $x = 0.40$  (Figure 1(d)). This contraction is consistent with the smaller ionic radius of  $F^-$  (1.31 Å) replacing  $O^{2-}$  (1.38 Å) in the SmO/F layers. These trends are similar to those reported for CSP-synthesised Sm1111 [6], as shown in Figures 1(c) and 1(d). The unit-cell volume  $V$  decreases nearly linearly with fluorine doping, from 130.7(1) Å<sup>3</sup> at  $x = 0.05$  to 129.4(1) Å<sup>3</sup> at  $x = 0.30$ , remaining nearly constant at 129.5(1) Å<sup>3</sup> for  $x = 0.40$ , as depicted in Figure 1(e), confirming effective incorporation of fluorine into the superconducting lattice. A direct comparison of the lattice parameters and lattice volume of CSP-prepared samples shows that our high-pressure samples exhibit slightly smaller  $a$ ,  $c$ , and  $V$  values at the matched fluorine compositions. This difference suggests a modestly higher and effective amount of fluorine inserted inside the superconducting lattice under high-pressure synthesis conditions. Moreover, our high-pressure synthesis extends the doping series to  $x = 0.30$  and  $0.40$ , where impurity reflections become more pronounced and the superconducting phase fraction decreases from ~82% to ~60%. This trend mirrors the impurity growth and reduced superconducting fraction as reported for Sm1111 samples with  $x = 0.25$  by CSP method [6]. Collectively, the XRD analysis confirms that the tetragonal 1111 structure is preserved across the studied doping range (up to 0.4), with lattice contraction as the dominant structural response to fluorine substitution. As a result, the unit-cell volume decreases nearly linearly with increasing  $x$ , while the impurity phases increase significantly beyond  $x \approx 0.25$ , in agreement with previous reports based on CSP process.

Microstructural characterization of the synthesized SmFeAsO<sub>1-x</sub>F<sub>x</sub> bulks was carried out on finely polished surfaces. Back-scattered electron (BSE) imaging was utilized to reveal both compositional contrast and microstructural morphology. The selected BSE images corresponding to the underdoped, optimal doped, and overdoped compositions are displayed in Figures 2(a)-(b), 2(c)-(d), and 2(e)-(f), respectively. In these micrographs, bright areas represent the impurity Sm<sub>2</sub>O<sub>3</sub> or SmOF phase, while the light grey matrix denotes the superconducting SmFeAs(O,F) phase, and the dark regions are normally attributed to pores. In some cases, the dark region can represent SmAs or FeAs as secondary phases. The underdoped sample ( $x = 0.05$ ) appears dense and largely single-phase, with only a few tiny bright inclusions. The optimally doped sample ( $x = 0.20$ ; Figure 2(c)) exhibits a more homogeneous and denser

microstructure compared to the underdoped sample. A small number of impurity phases, identified as SmAs and Sm<sub>2</sub>O<sub>3</sub>, are observed at a few locations, suggesting that both homogeneity and sample density are improved at 20% fluorine doping level. In the overdoped sample ( $x = 0.40$ ; Figure 2(e)), the secondary phases such as Sm<sub>2</sub>O<sub>3</sub>/SmOF become more abundant and coarser, many residing along grain boundaries and forming weak Josephson-junction-like morphologies, consistent with typical behavior in overdoped F-doped Sm1111 [35] and with XRD evidence of increased impurity formation at high fluorine content. High-magnification BSE images provide insight into grain-boundary (GB) quality. For  $x = 0.05$  (Figure 2(b)) and  $x = 0.20$  (Figure 2(d)), many grains are well-connected, and the grain boundaries are clean and continuous, with no observable impurity phases at the nanoscale. This indicates a good electrical percolation path of the current in these bulks. For  $x = 0.40$  (Figure 2(f)), the boundary network remains largely continuous; however, faint nanometer-scale contrasts appear more frequently at some interfaces, consistent with the presence of thin intergranular secondary phases. Overall, Figure 2 demonstrates that the high-pressure synthesis produces ~98% dense compacts with well-connected grain boundaries across the doping series. The gradual increase of Sm<sub>2</sub>O<sub>3</sub>/SmAs/SmOF content from optimal to overdoped compositions, as also observed in XRD, confirms the rise of impurity phases at high fluorine doping.

Raman spectra were collected at room temperature directly from the as-prepared polycrystalline samples, without any post-synthesis polishing or surface modification. Due to the polycrystalline morphology of the samples, noticeable variations were observed in the relative intensities of the spectral features, depending on the measurement location. This variability is likely associated with differences in grain orientation and local crystallographic alignment at the measurement sites. As a result, we did not pursue a detailed analysis of intensity trends related to fluorine doping, since such variations could not be unambiguously attributed to compositional effects alone. To account for statistical variation and ensure consistency in peak position identification, Raman measurements were performed at three distinct locations on each sample for a given fluorine concentration. The acquired spectra were then processed using peak deconvolution with Lorentzian functions, allowing for the accurate extraction of vibrational mode positions. For all prepared SmFeAsO<sub>1-x</sub>F<sub>x</sub> samples, the representative spectra from the underdoped, optimal doped, and overdoped regions are shown in Figure 3(a). The spectra reveal signals corresponding to lattice vibrations (phonons) of Sm, As, and Fe atoms, with A<sub>1g</sub>, A<sub>1g</sub>, and B<sub>1g</sub> symmetries, respectively, consistent with previous reports on pristine SmFeAsO, Cu-doped material (SmFe<sub>1-x</sub>Cu<sub>x</sub>AsO) and other similar *RE*-based oxypnictides [36,



37, 38, 39, 40]. For the fluorine-doped Sm1111, *i.e.*,  $\text{SmFeAsO}_{1-x}\text{F}_x$  ( $x = 0.05 - 0.40$ ), no major changes in the overall Raman spectra were observed, indicating that the crystal structure remains stable and the chemical bonding is largely unaffected by fluorine substitution, as depicted in Figure 3(b). Analysis of the peak positions reveals a pronounced softening (shift to lower frequency) of the Sm-related mode and considerable hardening (shift to higher frequency) of the Fe-related mode with increasing fluorine content, corresponding to a decrease and increase in Raman frequency of ca.  $8 \text{ cm}^{-1}$  and  $4 \text{ cm}^{-1}$ , respectively. In contrast, the As-related mode shows only minor shifts within experimental error. These trends in phonon frequency shifts upon fluorine doping are similar to those reported for  $\text{NdFeAsO}_{1-x}\text{F}_x$  ( $x = 0-0.2$ ) [40], reflecting subtle modifications in local bonding environments associated with electron doping through fluorine substitution.

The temperature-dependent resistivity of all prepared  $\text{SmFeAsO}_{1-x}\text{F}_x$  bulks ( $0.05 \leq x \leq 0.40$ ) is shown in Figure 4(a) up to room temperature under zero magnetic field. All compositions exhibit metallic behaviour from 300 K down to the superconducting transition, with nearly linear temperature dependence and no low-temperature upturns, indicating good grain connectivity and the absence of residual magnetic or structural anomalies reported for the parent  $\text{SmFeAsO}$  [6]. The underdoped samples ( $x = 0.05, 0.10, 0.20$ ) display only slight variations in the normal-state resistivity across the measured range, while further fluorine doping ( $x > 0.20$ ) leads to a systematic reduction in resistivity, which could be due to enhanced electron doping of the superconducting FeAs layers and reduced grain-boundary scattering in these densified bulks prepared by the CA-HP process.

The low-temperature resistivity of the samples ( $0.05 \leq x \leq 0.40$ ) is presented in Figure 4(b), where the onset transition temperature  $T_c^{\text{onset}}$  and offset transition temperature  $T_c^{\text{offset}}$  were determined using 90% and 10% of the respective normal-state resistivity. The underdoped samples show onset transition temperatures of  $\sim 54.4 \text{ K}$  and  $55.6 \text{ K}$  for  $x = 0.05$  and  $0.10$ , which is  $\sim 10\text{-}17 \text{ K}$  higher than reported for F-doped Sm1111 prepared by the CSP method [6]. In contrast, the  $T_c^{\text{onset}}$  ( $\sim 55\text{-}57 \text{ K}$ ) remains nearly constant in the optimal doped ( $0.20 \leq x \leq 0.25$ ) and overdoped ( $0.25 < x \leq 0.40$ ) regions, consistent with previous CSP reports [6], while the transition width ( $\Delta T$ ) is reduced in the samples prepared by the CA-HP method. The underdoped samples ( $x = 0.05\text{-}0.10$ ) exhibit slightly broader superconducting transitions, likely due to minor spatial variations in F-content and weaker intergrain coupling. Notably, the heavily doped sample ( $x = 0.40$ ) maintains a clear zero-resistance state below  $T_c$  but shows a modest reduction

in  $T_c^{onset}$  and mild broadening compared to the optimal doped samples, consistent with secondary-phase formation inferred from XRD and SEM analyses.

To further evaluate sample quality, we extracted the superconducting transition temperature  $T_c^{onset}$ , transition width  $\Delta T = T_c^{onset} - T_c^{offset}$ , room-temperature resistivity  $\rho_{300K}$ , and residual resistivity ratio  $RRR (= \rho_{300K} / \rho_{60K})$ , as shown in Figures 4(c)-(f) respectively. Figure 4(c) shows the variation of  $T_c^{onset}$  with nominal fluorine content ( $x$ ). The onset temperature increases from 54.4 K at  $x = 0.05$  to a maximum of 57.3 K at  $x = 0.20$ , then slightly decreases to 56.8 K ( $x = 0.25$ ), 56.3 K ( $x = 0.30$ ), and 55.5 K ( $x = 0.40$ ). The slight decrease of  $T_c^{onset}$  in the overdoped region may result from the increased presence of impurity phases, as suggested by structural analysis. The transition width  $\Delta T$  is large for underdoped samples, measuring 7.7 K at  $x = 0.05$  and 8.5 K at  $x = 0.10$ . However, it decreases nearly two- to threefold for the optimally doped sample, which has a transition width of 3 K at  $x = 0.20$ , reflecting improvements in sample density, intergrain connectivity, and a decrease in impurity content. For higher doping,  $\Delta T$  is 2.7 K at  $x = 0.25$  and slightly increases in the overdoped region (3.4 K at  $x = 0.30$  and 0.40), consistent with the formation of secondary phases. The room-temperature resistivity  $\rho_{300K}$  (Figure 4(e)) is  $\sim 1.8 \text{ m}\Omega\cdot\text{cm}$  for underdoped and optimally doped ( $x = 0.2$ ) samples, and decreases monotonically for higher fluorine contents ( $x = 0.25$ – $0.40$ ), suggesting increased carrier density and fewer effective scattering centres in these dense polycrystalline samples. The  $RRR$  (Figure 4(f)) shows a dome-like dependence on fluorine content: it rises rapidly with doping in the underdoped region, reaching a maximum of  $\sim 5.75$  at  $x = 0.20$ , then decreases to 4.97 ( $x = 0.25$ ), 4.65 ( $x = 0.30$ ), and 3.82 ( $x = 0.40$ ), indicating weaker homogeneity and intergrain connectivity in both underdoped and overdoped samples, likely due to the presence of the secondary phases as observed in the structural and microstructural analysis. Overall, this analysis indicates that a high  $T_c^{onset}$  along with a small  $\Delta T$  and a large  $RRR$ , is achieved within the optimal fluorine doping range  $x \approx 0.20$ – $0.25$ , where the dense and homogeneous F-doped Sm1111 can be obtained using the present high-pressure technique. The combination of resistivity and structural analysis suggests that  $T_c^{onset}$  generally increases as XRD peaks shift to higher  $2\theta$  values and the lattice constants contract with increasing fluorine content (Figures 1(b)-(e)). However, the continuous increase of  $T_c^{onset}$  is not observed (Figure 4(c)) with fluorine substitution, even with the steady contraction of the lattice parameters (Figure 1(c) and (d)). Fluorine substitution reduces the lattice size and injects electrons, and the observed  $T_c^{onset}$  exhibits a dome-shaped relationship with carrier concentration. We expect that near optimal doping ( $x \approx 0.20$ – $0.25$ ), the FeAs bands are tuned to

maximize  $T_c^{onset}$ , while further fluorine addition moves the system into the overdoped regime, where  $T_c^{onset}$  plateaus or declines. Simultaneously, higher fluorine doping promotes formation of secondary SmOF/SmAs/FeAs phases, as indicated by diffraction and scanning electron microscopy (SEM), and probably contribute to pair-breaking and intergranular scattering. These secondary phases reduce the effective superconducting cross-section and introduce weak links, consistent with the modest  $\Delta T$  broadening and  $RRR$  reduction for  $x \geq 0.3$ . Therefore, the observed plateau in  $T_c^{onset}$ , despite ongoing lattice contraction, likely results from surpassing the electronic optimum, while extrinsic scattering progressively increases, explaining a possibility why  $T_c^{onset}$  does not rise further with fluorine content in these F-doped SmFeAsO samples prepared by the CA-HP technique.

The variation of electrical resistivity ( $\rho$ ) with temperature was presented in Figure 5(a) for three fluorine compositions:  $x = 0.05$ ,  $0.25$ , and  $0.40$ , belonging to underdoped optimal doped and overdoped regions. These measurements were conducted under magnetic fields of up to 9 T within a temperature range of below 70 K. In the absence of an external field, each sample displayed a narrow superconducting transition, reflecting the compact and well-intergrain- connected microstructure as evident from SEM observations, along with metallic behavior in the normal state above  $T_c$ . With increasing field, the resistive transitions shift to lower temperatures; however, the transition broadening is minimal for  $x \approx 0.25$  compared with both the underdoped and overdoped samples. This behavior reflects the evolution of grain connectivity and phase purity with fluorine doping: near optimal F content, grains are more strongly coupled and impurity content is reduced, while at the dome edges ( $x = 0.05$ , and especially  $x = 0.40$ ), non-superconducting inclusions and weak links give rise to a distribution of local  $T_c$  values and vortex pinning energies, which manifests as broader superconducting transitions under applied magnetic fields. To quantify the superconducting phase boundaries, we employed standard resistive criteria relative to the normal-state resistivity  $\rho_n(T)$ : the field at which  $\rho(T, H) = 0.9 \rho_n(T)$  defines the upper critical field  $H_{c2}(T)$ , while the field at which  $\rho(T, H) = 0.1 \rho_n(T)$  defines the irreversibility field  $H_{irr}(T)$  (loss of macroscopic dissipation-free transport). Using these definitions, the  $H_{c2}(T)$  and  $H_{irr}(T)$  phase diagrams are constructed and shown in the inset of Figures 5(a)-(c) for the respective samples. From the data, the slopes  $(dH_{c2}/dT)|_{T_c}$  were determined as  $-17.3$ ,  $-5.7$ , and  $-3.2 \text{ T K}^{-1}$  for the  $x = 0.05$ ,  $0.25$ , and  $0.40$  samples, respectively. The upper critical field  $H_{c2}(0)$  was then estimated using the Werthamer–Helfand–Hohenberg (WHH) single-band orbital formula [41],  $\mu_0 H_{c2}(0) \approx -0.693 T_c (dH_{c2}/dT)|_{T=T_c}$ . Taking the resistive onset transition temperatures  $T_c^{onset}$  from transport measurements

at zero magnetic field (54.4 K, 56.8 K, and 55.5 K for  $x = 0.05$ , 0.25, and 0.40, respectively; Figure 4(c)), we have estimated zero-temperature upper critical fields of  $\mu_0 H_{c2}(0) \approx 223$  T for  $x = 0.25$  and  $\mu_0 H_{c2}(0) \approx 125$  T for  $x = 0.40$ . For the underdoped sample, we observe nearly double the upper critical field compared to the optimally doped sample, consistent with earlier reports on F-doped Sm1111 single crystals [7]. This behavior further supports the notion of more uniform pinning and stronger intergrain coupling in the optimal and underdoped Sm1111, making it a promising candidate for high-field applications. The corresponding Ginzburg–Landau coherence lengths were estimated from  $\mu_0 H_{c2}(0)$  using  $\xi(0) = \sqrt{[\Phi_0/(2\pi \mu_0 H_{c2}(0))]}$  [42], where  $\Phi_0$  is the flux quantum. The calculated values are  $\xi(0) \approx 0.71$  nm ( $x = 0.05$ ), 1.21 nm ( $x = 0.25$ ), and 1.71 nm ( $x = 0.40$ ). It is well established that high- $T_c$  iron-based superconductors are multiband in nature, and their upper critical field behavior can be understood within the framework of multiband  $s\pm$  pairing [43]. While the WHH model considers only orbital pair-breaking, real superconductors are strongly influenced by both orbital and spin paramagnetic effects. Their relative importance is quantified by the Maki parameter [44],  $\alpha = 1.44 H_{c2}^{orbital}(0) / H_{c2}^{para}(0)$ , where the spin paramagnetic limiting field is given by  $H_{c2}^{para}(0) = 1.84 T_c$  according to BCS theory [45]. The WHH-derived  $H_{c2}(0)$  values in our samples significantly exceed the spin paramagnetic limit, resulting in  $\alpha > 1$ , which suggests the possibility of a Fulde–Ferrell–Larkin–Ovchinnikov (FFLO) state [46]. It is also reported that in multiband superconductors, both  $H_{c2}^{orbital}$  and the stability of the FFLO state can be tuned by the doping type and level. This may explain the distinct  $H_{c2}(0)$  values as we observe across underdoped, optimal doped, and overdoped F-doped Sm1111 samples. Notably, experimental measurements of the 1111 family have reported upper critical fields up to 85 T [47], clearly highlighting the limitations of WHH extrapolations, which neglect spin-paramagnetic effects and the intrinsic multiband nature of these superconductors.

The field-induced broadening of the resistive transitions originates from dissipation caused by the motion of vortices in the mixed state. Under a transport current, each vortex experiences a Lorentz force; if the local pinning force dominates, vortex motion occurs only through thermally activated hopping (flux creep), whereas if the Lorentz force exceeds pinning, motion becomes viscous (flux flow) [48]. Within the temperature and field range of our measurements, the dissipation is governed by thermally activated flux flow (TAFF), where the resistivity follows an Arrhenius relation:  $\rho(T, H) = \rho_0 \exp[-U_0(H) / k_B T]$  with  $U_0$  as the effective pinning (activation) energy. Here, we have normalized the resistivity by the normal state resistivity ( $\rho_n$ ) i.e., just above the superconducting transition. Accordingly, Arrhenius plots of

$\ln(\rho / \rho_n)$  versus  $1/T$  display straight-line behavior in the TAFF regime, where the slope  $-U_0(H)/k_B$  provide the activation energy  $U_0(H)$  with different magnetic fields. Representative Arrhenius plots for the samples with  $x = 0.05, 0.25$ , and  $0.40$  under fields up to 9 T are shown in Figures 6(a)-(c). The nearly linear segments just below  $T_c$  confirm TAFF behavior, as shown in Figures (a)-(c). Increasing the magnetic field reduces the slope, reflecting the monotonic decrease of  $U_0$  with the magnetic field as the intervortex spacing shrinks and thermal hopping becomes easier. The field dependence of the activation energy  $U_0$  extracted from these slopes is summarized in Figure 6(d) for all these samples. The field dependence of the activation energy follows a power law,  $U_0(H) \propto H^{-\eta}$ , a characteristic signature of collective vortex dynamics. A weak field dependence of  $U_0$  at low fields reflects dominant single-vortex pinning, followed by stronger field dependence once the intervortex spacing becomes comparable to or smaller than the penetration depth, marking the onset of collective creep in high fields [49]. For the underdoped sample ( $x = 0.05$ ), two distinct regimes are evident:  $\eta \approx 0.29$  at low fields and  $\eta \approx 0.50$  at higher fields, indicating a crossover from single-vortex (or small-bundle) creep to more collective or plastic creep as the vortex density increases. The optimal doped sample ( $x = 0.25$ ) shows a similar behavior, with  $\eta \approx 0.38$  in the low-field region and  $\eta \approx 0.44$  at higher fields. In contrast, the overdoped sample ( $x = 0.40$ ) exhibits  $\eta \approx 0.42$  at low fields (up to 3 T) and  $\eta \approx 0.51$  at higher fields, reflecting the most pronounced suppression of  $U_0$  with field in the low-field regime and, consequently, the weakest effective pinning landscape among the studied compositions. The weak field dependence of the coefficient  $\eta$  in both low- and high-field regions for the optimal doped sample indicates superior grain connectivity and overall sample quality compared to the underdoped and overdoped Sm1111 samples. This evolution of  $\eta$  is consistent with reports on other iron-based superconductors (e.g., Nd1111, Sm1111, FeSe) [49] [50]. In our polycrystalline bulks, the absolute values of  $U_0$  are smaller than those reported for F-doped Sm1111 single crystals [7] because grain boundaries and secondary phases reduce the effective superconducting cross-section and introduce weak links, thereby limiting both the macroscopic pinning force and the field dependence of the critical current.

The magnetic susceptibility of all prepared samples is measured in zero-field-cooled (ZFC) and field-cooled (FC) modes under an applied field of 20 Oe in the temperature range of 5–60 K, and the normalized magnetization as a function of temperature is presented in Figure 7(a). All SmFeAsO<sub>1-x</sub>F<sub>x</sub> bulks exhibit a clear diamagnetic response for each composition, confirming bulk superconductivity in these polycrystalline samples. Normalization of the magnetization enables direct comparison of the superconducting transition behavior across

different fluorine substitution levels. The underdoped samples ( $x = 0.05$  and  $0.10$ ) display the broadest transitions in the ZFC mode along with a pronounced ZFC-FC separation extending well below  $T_c$ . The transition temperatures are observed at approximately 50 K for  $x = 0.05$  and 51 K for  $x = 0.10$ . The broad transitions and the presence of a double-step feature suggest weaker intergranular coupling and a wider distribution of local superconducting transition temperatures. In contrast, the  $x = 0.20$  sample, which belongs to the optimally doped region, exhibits an onset transition at 56 K with a clear double-step feature. The  $x = 0.25$  sample exhibits an almost single-step transition with an onset at 55 K, indicative of improved grain connectivity compared with the  $x = 0.05$ ,  $0.10$ , and  $0.20$  samples. With further fluorine doping ( $x = 0.30$  and  $0.40$ ), the transitions broaden again and display double-step features, although the onset temperature remains around 54 K. Interestingly, the higher-doped  $x = 0.40$  sample still develops a robust diamagnetic state, albeit with a slightly lower onset temperature and modest broadening compared to the sample  $x \approx 0.25$ . The observed transition temperatures are  $\sim 1$  K lower than those determined from transport measurements, as discussed above. Slightly negative FC branches are observed for all fluorine-doped samples, reflecting strong vortex pinning and irreversible flux trapping [39]. The maximum transition temperature for  $x \approx 0.20$ – $0.25$  coincides with the narrowest resistive transitions and the highest residual resistivity ratio ( $RRR$ ). In contrast, the highest fluorine-doped sample ( $x = 0.40$ ) shows a slightly reduced  $T_c$  and broader transitions, likely due to the presence of secondary SmAs/Sm<sub>2</sub>O<sub>3</sub> phases, as revealed by structural and microstructural analysis. These non-superconducting inclusions reduce the effective cross-sectional area and introduce weak links at some grain boundaries, even though the pellets remain overall dense and well-connected.

A high critical current density ( $J_c$ ) is essential for the technological application of a superconducting material. To evaluate this parameter, magnetic hysteresis ( $M$ - $H$ ) measurements were conducted at 5 K under the magnetic fields up to 9 T for all prepared bulks. The hysteresis width ( $\Delta M$ ), defined as the difference between the magnetic moments recorded during the increasing and decreasing field cycles, was used to estimate  $J_c$  according to the extended Bean model:  $J_c = 20\Delta m/Va(1-a/3b)$ , where  $a$  and  $b$  denote the in-plane dimensions of the sample ( $a < b$ ), and  $V$  represents the sample volume. [51]. The calculated  $J_c$  at 5 K as a function of applied magnetic field is shown in Figure 7(b) for samples with  $x = 0.05$ ,  $0.10$ ,  $0.20$ ,  $0.25$ ,  $0.3$  and  $0.4$ . The sample with  $x = 0.05$  exhibits high  $J_c$  values at low fields, which decrease rapidly with increasing magnetic field and reach approximately  $10^3$  A/cm<sup>2</sup> at 3 T, remaining nearly constant up to 9 T. Overall, the  $J_c$  of the  $x = 0.05$  sample remains around  $3 \times 10^3$  A/cm<sup>2</sup> across the entire

magnetic field range, which is higher than that reported for underdoped F-doped Sm-1111 prepared by the CSP method [6]. The behavior of the  $x = 0.10$  sample is similar to that of  $x = 0.05$ , with  $J_c$  values increased by approximately  $1 \times 10^3$  A/cm<sup>2</sup> throughout the entire magnetic field range. With further fluorine doping ( $x = 0.20$ ), the  $J_c$  value and its field dependence remain nearly the same as for the  $x = 0.10$  sample. A significant enhancement is observed for the  $x = 0.25$  sample, where  $J_c$  increases by approximately an order of magnitude at low magnetic fields, though it decreases by about 4000 A/cm<sup>2</sup> under fields up to 9 T. In contrast, the  $x = 0.30$  and  $x = 0.40$  samples, which lie in the overdoped region, exhibit reduced  $J_c$  compared with  $x = 0.25$ . Notably, these overdoped samples also exhibit a significantly faster degradation of  $J_c$  with the magnetic field, likely due to the presence of impurity phases, as corroborated by the XRD and transport measurements discussed above. Interestingly, the  $J_c$  values of the samples prepared by the high-pressure method exhibit robust behavior against magnetic fields, which is highly favorable for magnetic applications. The  $x = 0.40$  sample shows the fastest suppression of  $J_c$  with increasing field, attributable to the larger population of SmAs/Sm<sub>2</sub>O<sub>3</sub> impurity phases decorating the grain boundaries and forming Josephson junctions. These features, directly observed in SEM images, disrupt the superconducting network and reduce the effective intergranular critical current under high Lorentz forces. To gain further insight into the  $J_c$  performance, the flux pinning force ( $F_p$ ) was calculated using the relation  $F_p = \mu_0 H \times J_c$  [52], as shown in the inset of Figure 7(b). The analysis confirms an enhanced pinning force for the  $x = 0.25$  sample compared with the other compositions, indicating that increased flux pinning contributes to its superior  $J_c$ . Overall, the obtained  $J_c$  values are an order of magnitude higher, with improved field robustness, compared with those reported for F-doped Sm-1111 synthesized by the CSP method.

## Discussion:

The composition dependence of the superconducting properties of SmFeAsO<sub>1-x</sub>F<sub>x</sub> prepared via the CA-HP route is summarized in Figures 8(a) and 8(b), showing the superconducting onset transition  $T_c$  from transport measurements and the critical current density  $J_c$  from magnetic measurements. For comparison,  $T_c$  and  $J_c$  data for F-doped Sm1111 synthesized by the CSP method reported by Singh *et al.* [6] and Wang *et al.* [23] are also included in Figure 8 to evaluate the effects of growth conditions. Wang *et al.* had used the high-temperature ( $\sim 1200^\circ\text{C}$ ) synthesis process of F-doped Sm1111, whereas Singh *et al.* had used the low-temperature ( $\sim 900^\circ\text{C}$ ) synthesis process for the preparation of F-doped Sm1111. The

high-temperature CSP samples exhibit significantly lower  $T_c^{onset}$  than low-temperature CSP samples at the same fluorine content (Figure 8(a)), which suggests the evaporation of fluorine at the high-temperature synthesis process that is reduced by the low temperature synthesis process. F-doped Sm1111 synthesized by CA-HP shows a substantially higher  $T_c$  in the underdoped region, with a  $\sim 17$  K increase for  $x = 0.05$  and a  $\sim 13$  K increase for  $x = 0.10$  compared to CSP samples, while in the optimally doped region ( $x \approx 0.20$ – $0.25$ ),  $T_c^{onset}$  is comparable for both methods. In the overdoped region ( $x > 0.25$ ),  $T_c$  for CA-HP samples decreases slightly by 1-2 K relative to CSP samples. Overall, the CA-HP process enhances  $T_c$  by 10-17 K in the underdoped regime, while  $T_c$  remains nearly constant ( $\sim 55$ - $57$  K) in the optimal and overdoped regions ( $0.20 \leq x \leq 0.40$ ), either by CSP or CA-HP methods. Structural analysis reveals that CA-HP processed samples exhibit slightly smaller lattice parameters and unit-cell volumes (Figure 1) compared to CSP processed samples at the same fluorine content, indicating more effective fluorine incorporation within the superconducting lattice and improved densification due to the CA-HP process. The overdoped region promotes the formation of secondary phases (SmOF, SmAs, FeAs) at grain boundaries, which reduce the effective superconducting volume and weaken intergranular coupling. The combination of overdoping, slight geometric detuning, and increased boundary impurities likely accounts for the modest decrease in  $T_c$  in the overdoped region [5].

Figure 8(b) presents the critical current density ( $J_c$ ) at 5 K as a function of nominal fluorine composition ( $x$ ) for our samples, alongside previous CSP-based reports [6] [23]. F-doped samples prepared by low-temperature CSP exhibited maximum  $J_c$  values on the order of  $10^3$  A/cm<sup>2</sup> in the underdoped and optimal doped regions [6], while high-temperature CSP samples reached  $\sim 10^4$  A/cm<sup>2</sup> at optimal doping ( $x = 0.20$ ) [6], with a slight decrease in the overdoped region. For high-pressure synthesized samples,  $J_c$  shows a dome-like behavior, reaching a maximum at  $x = 0.25$  in the optimally doped region. In the underdoped region,  $J_c$  is slightly lower but remains higher than that of CSP-processed samples (Figure 8(b)), limited primarily by reduced carrier density and weaker intergranular coupling. On the higher-doped side,  $J_c$  decreases due to the increasing presence of impurity phases such as SmAs and Sm<sub>2</sub>O<sub>3</sub>, as well as the formation of Josephson junctions at grain boundaries, which disrupt the percolation pathways and accelerate the field-induced decay of  $J_c(H)$  in the samples grown under HP conditions. Compared with CSP method, our HP-grown samples exhibit  $J_c$  values of the same order of magnitude as those reported for the high-temperature CSP process at equivalent fluorine doping levels, as shown in Figure 8(b). The phase diagram shown in Figure



8 highlights a practical processing window for F-doped SmOFeAs at  $x \approx 0.25$ -0.30, where both  $T_c^{onset}$  and  $J_c$  are maximized through HP growth. High-pressure synthesis significantly enhances the superconducting properties across the entire underdoped region by stabilizing fluorine in the lattice and improving sample density, whereas the overdoped side remains limited by inhomogeneity and the presence of impurity phases. These correlations reduced lattice parameters and improved densification resulting from HP synthesis indicate a  $T_c$  behavior governed by the carrier–lattice geometry balance, and a  $J_c$  dome controlled by flux pinning, which is linked to phase purity and grain connectivity. Together, these insights provide a coherent framework for optimizing Sm-1111 bulk materials for current transport applications.

Overall, these studies indicate that HP synthesis is a highly effective method for underdoped samples, enhancing the onset transition temperature by approximately 17 K and increasing  $J_c$  by nearly an order of magnitude compared with CSP method [6]. The HP growth route simultaneously improves both the superconducting transition and the critical current properties, whereas the CSP process typically optimizes only one of these parameters in a single processing route. For instance, low-temperature CSP synthesis enhances the superconducting transition temperature but yields a lower  $J_c$  ( $\sim 10^3$  A/cm<sup>2</sup>), while high-temperature CSP synthesis increases  $J_c$  by an order of magnitude ( $\sim 10^4$  A/cm<sup>2</sup>) at the expense of reducing  $T_c$  by  $\sim 10$  K. Our HP synthesis approach shows promise for tape and wire applications by simultaneously controlling the superconducting transition and critical current. Nevertheless, further optimization and investigation are still required in this direction.

## Conclusion:

A series of polycrystalline SmFeAsO<sub>1-x</sub>F<sub>x</sub> bulks with  $0.05 \leq x \leq 0.40$  were synthesized using an *in-situ* CA-HP method and systematically characterized by structural, microstructural, Raman analysis, transport, and magnetic measurements. Structural analysis confirmed the stabilization of the tetragonal 1111 phase (*P4/nmm*) across the entire doping range, accompanied by a systematic contraction of the lattice parameters and unit-cell volume, indicative of effective fluorine incorporation. At equivalent fluorine concentrations, Sm1111 synthesized by the HP method exhibits slightly smaller lattice parameters and unit-cell volumes compared to samples prepared by the CSP method. This indicates that the HP method is more effective in promoting fluorine incorporation into the superconducting lattice, while simultaneously enhancing sample densification. Backscattered electron imaging at high

resolution revealed dense microstructures with clean and well-connected grain boundaries in the optimal doped region, whereas the overdoped samples ( $x > 0.25$ ) showed secondary phases such as SmOF, Sm<sub>2</sub>O<sub>3</sub>, and SmAs accumulating at grain boundaries, potentially degrading intergranular connectivity. Transport and magnetization measurements confirmed bulk superconductivity across the doping range up to  $x = 0.4$ , with a dome-like dependence of  $T_c$  and  $J_c$  on fluorine content. The optimal doped compositions ( $x \approx 0.20$ -0.25) exhibited the highest performance, achieving  $T_c$  of ~55-57 K and  $J_c \sim 10^4$  A cm<sup>-2</sup>, with  $J_c$  remaining nearly field-independence at high fields. Analysis of the upper critical field  $H_{c2}(0)$  indicated the dominance of the Pauli paramagnetic effect, consistent with short coherence lengths (~1–2 nm) and the multiband character of Sm1111. Thermally activated flux-flow behavior revealed a power-law field dependence of the activation energy,  $U_0(H) \propto H^{-\eta}$ , across all doping regions, suggesting collective vortex pinning at high magnetic fields (>3 T). These results demonstrate that high-pressure synthesis is a highly effective strategy for enhancing both  $T_c$  and  $J_c$  compared with conventional methods. The CA-HP process enables the preparation of dense, homogeneous, and high-performance Sm1111 bulks, underscoring their strong potential for practical superconducting wire and tape applications.

## CRediT authorship contribution statement

**Mohammad Azam:** Writing – review & editing, Writing – original draft, Investigation, Formal analysis, Data curation. **Tatiana Zajarniuk:** Data curation, Investigation, Resources, Writing – review & editing. **Ryszard Diduszko:** Formal analysis, Investigation, Resources, Data curation, Writing – review & editing. **Taras Palasyuk:** Writing – review & editing, Formal analysis, Investigation, Data curation. **Cezariusz Jastrzębski:** Writing – review & editing, Resources, Data curation. **Andrzej Szewczyk:** Writing–review & editing, Resources, Data curation. **Hiraku Ogino:** Writing–review & editing, Investigation, Resources, Methodology. **Shiv J. Singh:** Writing–review & editing, Writing – original draft, Visualization, Validation, Supervision, Software, Resources, Methodology, Investigation, Funding acquisition, Formal analysis, Conceptualization.

## Declaration of competing interest

The authors declare that they have no known competing financial interests or personal relationships that could have appeared to influence the work reported in this paper.

## **Data availability**

The raw/processed data required to reproduce these findings cannot be shared at this time due to technical or time limitations. Data are available upon request to the corresponding author.

## **Acknowledgments:**

The work was funded by SONATA-BIS 11 project (Registration number: 2021/42/E/ST5/00262) sponsored by National Science Centre (NCN), Poland. SJS acknowledges financial support from National Science Centre (NCN), Poland through research Project number: 2021/42/E/ST5/00262. We would like to acknowledge H. Kito, AIST for his assistance during the experiments with cubic anvil high-pressure (CA-HP) techniques.

## References

- [1] Y. Kamihara, T. Watanabe, M. Hiran, H. Hosono, “Iron-Based Layered Superconductor La[O<sub>1-x</sub>F<sub>x</sub>]FeAs ( $x = 0.05\text{--}0.12$ ) with  $T_c = 26\text{ K}$ ,” *J. Am. Chem. Soc.*, vol. 130, p. 3296, 2008.
- [2] H. Hosono, K. Kuroki, “Iron-based superconductors: Current status of materials and pairing mechanism,” *Physica C*, vol. 514, p. 399–422, 2015.
- [3] Hideo Hosono, Kazuhiko Kuroki, “Iron-based superconductors: Current status of materials and pairing,” *Physica C*, vol. 514, p. 399–422, 2015.
- [4] Chiheng Dong, Qingjin Xu and Yanwei Ma, “Towards high-field applications: high-performance, low-cost iron-based superconductors,” *Natl Sci Rev*, vol. 11, pp. 1-20, 2024.
- [5] M. Fujioka, S. J. Denholme, T. Ozaki, H. Okazaki, K. Deguchi, S. Demura, H. Hara and e. al, “Phase diagram and superconductivity at 58.1 K in  $\alpha$ -FeAs-free SmFeAsO<sub>1-x</sub>F<sub>x</sub>,” *Supercond. Sci. Technol.*, vol. 26, p. 085023, 2013.
- [6] S. J. Singh, J. Shimoyama, . A. Yamamoto, H. Ogino and . K. Kishio, ““Transition temperature and upper critical field in SmFeAsO<sub>1-x</sub>F<sub>x</sub> synthesized at low heating temperatures”, IEEE Transactions on Applied Superconductivity,” vol. 23, p. 2239352, 2013.
- [7] Fujioka et al., “The effect of exceptionally high fluorine doping on the anisotropy of single crystalline SmFeAsO<sub>1-x</sub>F<sub>x</sub>,” *Appl. Phys. Lett.*, vol. 105, p. 102602, 2014.
- [8] X.C. Wang, et al, “Revisiting the electron-doped SmFeAsO: enhanced superconductivity up to 58.6 K by Th and F codoping,” *Chin. Phys. Lett.*, vol. 34, p. 077401, 2017.
- [9] Jun-ichi Shimoyama, “Potentials of iron-based superconductors for practical future materials,” *Supercond. Sci. Technol.*, vol. 27, p. 044002, 2014.
- [10] S. J. S. a. M. I. Sturza, “Bulk and Single Crystal Growth Progress of Iron-Based Superconductors (FBS): 1111 and 1144,” *Crystals*, vol. 12, pp. 1-22, 2022.
- [11] David C. Johnston, “The puzzle of high temperature superconductivity in layered iron pnictides and chalcogenides,” *Adv Phys.*, vol. 59, pp. 803-61, 2010.
- [12] J. Karpinski et. al, “Single crystals of LnFeAsO<sub>1-x</sub>F<sub>x</sub> (Ln = La, Pr, Nd, Sm, Gd) and Ba<sub>1-x</sub>Rb<sub>x</sub>Fe<sub>2</sub>As<sub>2</sub>: Growth, structure and superconducting properties,” *Physica C: Superconductivity*, vol. 469, pp. 370-380, 2009.
- [13] J. Paglione, R. Greene, , “High-temperature superconductivity in iron-based materials,” *Nature Physics*, vol. 6, pp. 645-658, 2010. .
- [14] J. ZHAO et al, “Structural and magnetic phase diagram of CeFeAsO<sub>1-x</sub>F<sub>x</sub> and its relation to high-temperature superconductivity,” *nature materials*, vol. 7, p. 953, 2008.
- [15] Kapil Ingle, K R Priolkar, Anand Pal, V P S Awana and S Emura, “Local structural distortions and their role in superconductivity in SmFeAsO<sub>1-x</sub>F<sub>x</sub> superconductors,” *Supercond.Sci.Technol.*, vol. 27, p. 075010, 2014.

- [16] Kazuhiko Kuroki et al, “Unconventional Pairing Originating from the Disconnected Fermi Surfaces of Superconducting  $\text{LaFeAsO}_{1-x}\text{F}_x$ ,” *Phys. Rev. Lett.* , vol. 101, p. 087004, 2008.
- [17] X. Chen, P. Dai, D. Feng, T. Xiang, F. Zhang, “Iron-based high transition temperature superconductors,” *National Science Review*, vol. 1, p. 371–395, 2014.
- [18] P J Hirschfeld, M. M. Korshunov, and I I Mazin, “Gap symmetry and structure of Fe-based,” *Rep. Prog. Phys.*, vol. 74 , p. 124508, 2011.
- [19] S. V. Borisenko et. al, “Direct observation of spin–orbit coupling in iron-based superconductors,” *Nature Physics* , vol. 12, pp. 311-317, 2016.
- [20] Chul-Ho LEE et al, “ Effect of Structural Parameters on Superconductivity,” *J.Phys.Soc. Jpn*, vol. 77, p. 083704, 2008.
- [21] K. Kuroki H. Usui, S. Onari, Ryotaro Arita, and H. Aoki, “Pnictogen height as a possible switch between high- $T_c$  nodeless and low- $T_c$  nodal pairings in the iron-based superconductors,” *Physical Review B* , vol. 79, p. 224511, 2009.
- [22] C. Lee, K. Kihou, A. Iyo, H. Kito, P. Shirage, H. Eisaki, “Relationship between crystal structure and superconductivity in iron-based superconductors,” *Solid State Communications* , vol. 152, p. 644–648, 2012 .
- [23] Chunlei Wang et al, “Low-temperature synthesis of  $\text{SmO}_{0.8}\text{F}_{0.2}\text{FeAs}$  superconductor with  $T_c = 56.1$  K,” *Supercond. Sci. Technol.*, vol. 23, p. 055002, 2010.
- [24] P. Singh, M. Manasa, M. Azam and S. J. Singh, “High-pressure growth effect on the properties of high- $T_c$  iron-based superconductors: A short review,” *Cryogenics*, vol. 147, p. 104028, 2025.
- [25] M. Azam, M. Manasa, A. Morawski, T. Cetner , S. J. Singh, “High Gas Pressure and High-Temperature Synthesis (HP-HTS) Technique and Its Impact on Iron-Based Superconductors,” *Crystals*, vol. 13, p. 1525, 2023.
- [26] N. D. Zhigadlo et al, “High-pressure flux growth, structural, and superconducting properties of  $\text{LnFeAsO}$  ( $\text{Ln} = \text{Pr}, \text{Nd}, \text{Sm}$ ) single crystals,” *Phys. Rev. B*, vol. 86, p. 214509 , 2012.
- [27] Ren Zhi-An et al., “Superconductivity at 55 K in Iron-Based F-Doped Layered Quaternary Compound  $\text{Sm}[\text{O}_{1-x}\text{F}_x]\text{FeAs}$ ,” *CHIN.PHYS.LETT.*, vol. 25, p. 2215, 2008.
- [28] Zhi-An Ren et. al, “Superconductivity in the iron-based F-doped layered quaternary compound  $\text{Nd}[\text{O}_{1-x}\text{F}_x]\text{FeAs}$ ,” *EPL*, vol. 82, p. 57002, 2008.
- [29] Z. Ren, Z. Zhao, “Research and prospects of iron-based superconductors,” *Adv. Mater.*, vol. 21, pp. 4584-4592, 2009.
- [30] M. Azam, T. Zajarniuk, H. Ogino, S. J. Singh, “Optimization of superconducting properties of F-doped  $\text{SmFeAsO}$  by cubic anvil high-pressure technique,” *Materials Research Express*, 2015, DOI 10.1088/2053-1591/ae1719,.
- [31] M. Azam, . M. Manasa, T. Zajarniuk, R. Diduszko, T. Palasyuk , T. Cetner, A. Morawski, C. Jastrzębski, A. Szewczyk, M. Wierzbicki and S. J. Singh , “High-pressure growth effects on the superconducting properties of Sm-based oxypnictides superconductors,” *Ceram. Int.*, vol. 51, pp. 13734-13751, 2025.

- [32] M. Azam, T. Zajarniuk, K. Kwatek, P. Mele, S. J. Singh, “Effect of spark plasma sintering on the superconducting properties of Sm-based oxypnictide,” *Cryogenics*, vol. 150, p. 104125, 2025.
- [33] P.M. Shirage et. al., “High-pressure synthesis and physical properties of new iron (nickel)-based,” *Physica C*, vol. 469, p. 355–369, 2009.
- [34] P. Quebe, L. J. Terbüchte, W. Jeitschko, “Quaternary rare earth transition metal arsenide oxides RTAsO (T=Fe, Ru, Co) with ZrCuSiAs type structure,” *J. Alloys Compd.*, vol. 302, pp. 70-74, 2000.
- [35] K. Iida, J. H. anisch, A. Yamamoto, “Grain boundary characteristics of Fe-based superconductors,” *Supercond. Sci. Technol.* , vol. 043001, p. 33, 2020.
- [36] V. G. Hadjiev, M. N. Iliev, K. Sasmal, Y.-Y. Sun, C. W. Chu, , “Raman spectroscopy of RFeAsO (R\_Sm, La),” *Phys. Rev. B*, vol. , vol. 77, p. 220505R, 2008..
- [37] C. Marini, C. Mirri, G. Profeta, S. Lupi, D. Di Castro, R. Sopracase, P. Postorino, P. Calvani, A. Perucchi, S. Massidda, G. M. Tropeano, M. Putti, A. Martinelli, A. Palenzona and P. Dore., “The optical phonon spectrum of SmFeAsO,” *Europhysics Letters*, vol. 84, p. 67013, 2008.
- [38] L. Zhang, P. F. Guan, D. L. Feng, X. H. Chen, S. S. Xie, M. W. Chen, “Spin-Dependent Electron–Phonon Interaction in SmFeAsO by Low-Temperature Raman Spectroscopy,” *J. Am. Chem. Soc.*, vol. 132, p. 15223–15227, 2010.
- [39] M. Azam et. al., “Copper doping effects on the superconducting properties of Sm-based oxypnictides,” *J. Am. Ceram. Soc.*, vol. 107, pp. 6806-6820, 2024.
- [40] L. Zhang, T. Fujita, F. Chen, D. L. Feng, S. Maekawa, M. W. Chen., “ Doping and temperature dependence of Raman scattering from NdFeAsO<sub>1-x</sub>F<sub>x</sub> (x=0–0.2) superconductor,” *Phys. Rev. B*, vol. 2009, p. 052507, 79.
- [41] N. R. Werthamer, E. Helfand, and P. C. Hohenberg, “Temperature and purity dependence of the superconducting,” *Phys. Rev.*, vol. 147 , p. 295–302, 1966.
- [42] E H Brandt, “The flux-line lattice in superconductors,” *Rep. Prog. Phys.* , vol. 58, p. 1465–594, 1995.
- [43] I. I. Mazin, D. J. Singh, M. D. Johannes, and M. H. Du, “Unconventional Superconductivity with a Sign Reversal in the Order Parameter of LaFeAsO<sub>1-x</sub>F<sub>x</sub>,” *Phys. Rev. Lett.* , vol. 101, p. 057003, 2008.
- [44] K. Maki, “Effect of Pauli paramagnetism on magnetic properties of high-field superconductors,” *Phys. Rev.*, vol. 148, p. 362–369, 1996.
- [45] J. Bardeen, L. N. Cooper, and J. R. Schrieffer, “Theory of Superconductivity,” *Phys. Rev.*, vol. 108, p. 1175, 1957.
- [46] A. Gurevich, , “Upper critical field and the Fulde-Ferrel-Larkin Ovchinnikov transition in multiband superconductors,” *Phys. Rev. B*, vol. 82, pp. 184504-1–184504-14,, 2010.
- [47] Hyun-Sook Lee et al, “Effects of two gaps and paramagnetic pair breaking on the upper critical field of SmFeAsO<sub>0.85</sub> and SmFeAsO<sub>0.8</sub>□<sub>0.2</sub> single crystals,” *Phys. Rev. B* , vol. 80, p. 144512, 2009.

- [48] AGurevich, “Iron-based superconductors at high magnetic fields,” *Rep. Prog. Phys.*, vol. 74 , p. 124501 , 2011.
- [49] G. Prando, P. Carretta, R. D. Renzi, S. Sanna, A. Palenzona, M. Putti, and M. Tropeano, “Vortex dynamics and irreversibility line in optimally doped  $\text{SmFeAsO}_{0.8}\text{F}_{0.2}$  from ac susceptibility and magnetization measurements,” *Phys. Rev. B*, vol. 2011 , p. 174514, 83.
- [50] J. Jaroszynski et al, “Comparative high field magnetotransport of the oxypnictide superconductors  $\text{RFeAsO}_{1-x}\text{F}_x$  ( $\text{R} = \text{La}, \text{Nd}$ ) and  $\text{SmFeAsO}_{1-\delta}$ ,” *Phys. Rev. B*, vol. 78, p. 064511, 2008.
- [51] C. P. Bean, “Magnetization of High-Field Superconductors,” *Rev. Mod. Phys.*, vol. 36, p. 31, 1964.
- [52] D Dew-Hughes, “Flux pinning mechanisms in type II superconductors,” *Philosophical Magazine*, vol. 30, pp. 293-305, 1974.

**Figure 1.** (a) Powder X-ray diffraction (XRD) patterns of  $\text{SmFeAsO}_{1-x}\text{F}_x$  samples ( $0.05 \leq x \leq 0.40$ ) synthesized under high pressure, showing the predominant tetragonal phase along with minor impurity phases identified as SmOF, SmAs, and FeAs. (b) Enlarged view of the (102) diffraction peak around  $2\theta \approx 31^\circ$ , illustrating the systematic peak shift towards higher angles with increasing fluorine content, consistent with lattice contraction caused by F substitution at oxygen sites. The variation of (c) lattice parameter ‘ $a$ ’ (d) lattice parameter ‘ $c$ ’ (e) unit-cell volume ‘ $V$ ’ as a function of nominal fluorine doping content ( $x$ ) for the synthesized  $\text{SmFeAsO}_{1-x}\text{F}_x$  bulks.

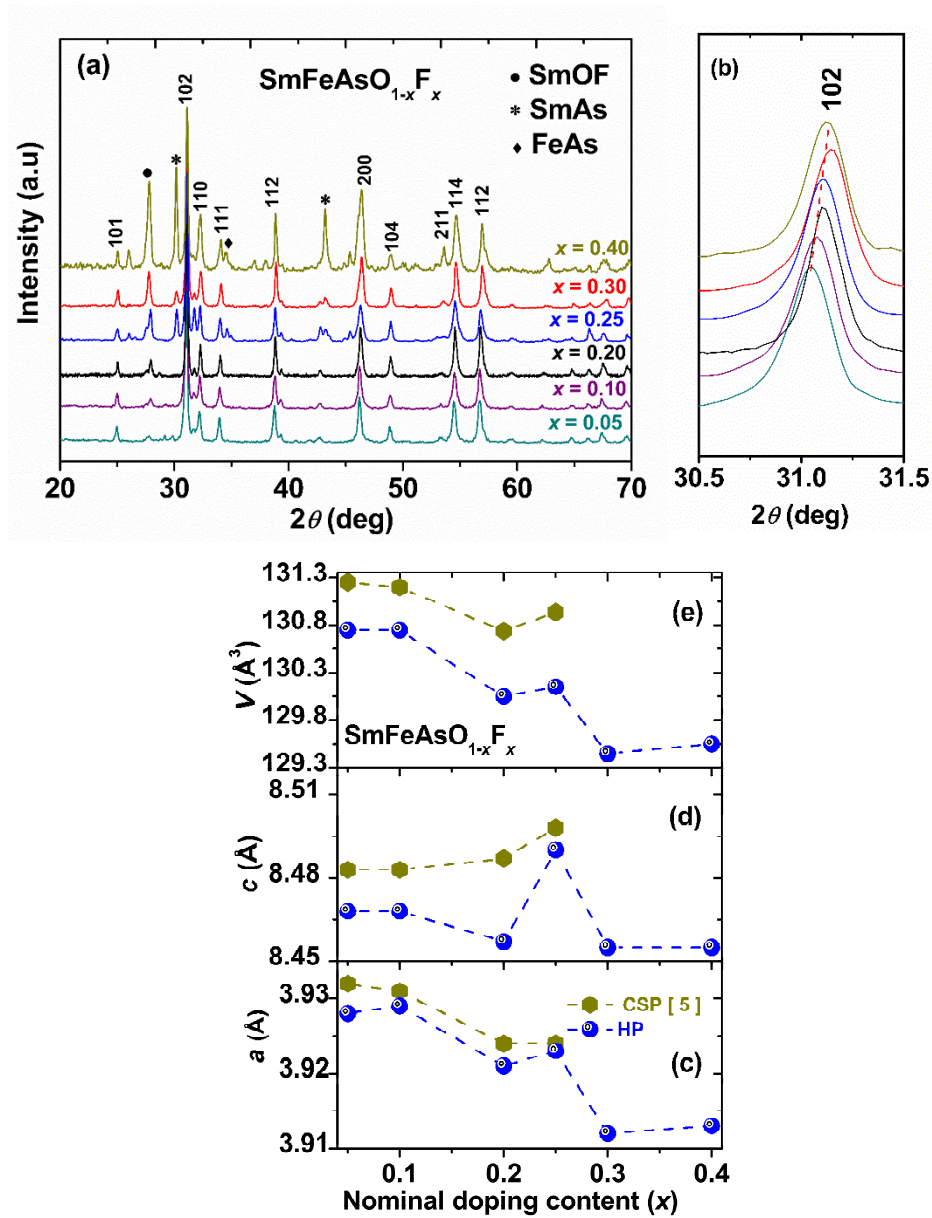




**Figure 2.** Backscattered electron (BSE) images of the representative  $\text{SmFeAsO}_{1-x}\text{F}_x$  samples from the underdoped ( $x = 0.05$ ), optimal doped ( $x = 0.20$ ), and overdoped ( $x = 0.40$ ) regions. Images for  $x = 0.05$ ,  $0.20$ , and  $0.40$  are shown at low magnification ( $10\ \mu\text{m}$ ; panels (a),(c),(e)) and higher magnification ( $200\ \text{nm}$ ; panels (b),(d),(f)). Bright, grey, and black contrasts correspond to  $\text{Sm}_2\text{O}_3/\text{SmOF}$ ,  $\text{SmFeAs}(\text{O},\text{F})$ , and  $\text{SmAs}$  phases, respectively. In some regions, the black contrast may also represent pores or the phase  $\text{SmAs}/\text{FeAs}$ .

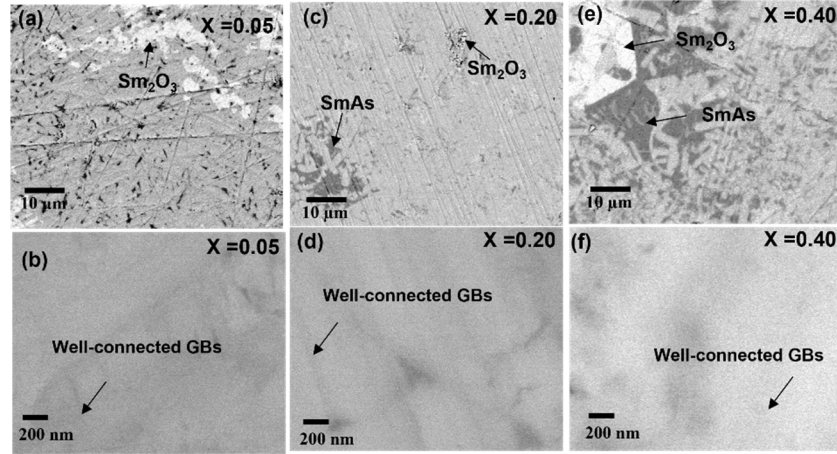


**Figure 3:** Raman scattering analysis of  $\text{SmFeAsO}_{1-x}\text{F}_x$ . **(a)** Representative Raman spectra for samples with fluorine concentrations of 5% ( $x = 0.05$ ), 20% ( $x = 0.20$ ), and 40% ( $x = 0.40$ ) are presented, with each spectrum vertically displaced for better visualization. The vibrational modes corresponding to the crystal lattice are identified for the underdoped specimen. Experimental spectra were deconvoluted using Lorentzian functions, represented by green curves, while the overall Lorentzian fits to the data are depicted in red. Vertical black markers are included as visual guides. **(b)** Variation of Raman peak positions with fluorine substitution is illustrated, where the experimental values (circles) are accompanied by associated error bars. The dashed lines serve only as visual guides to indicate the general trend.

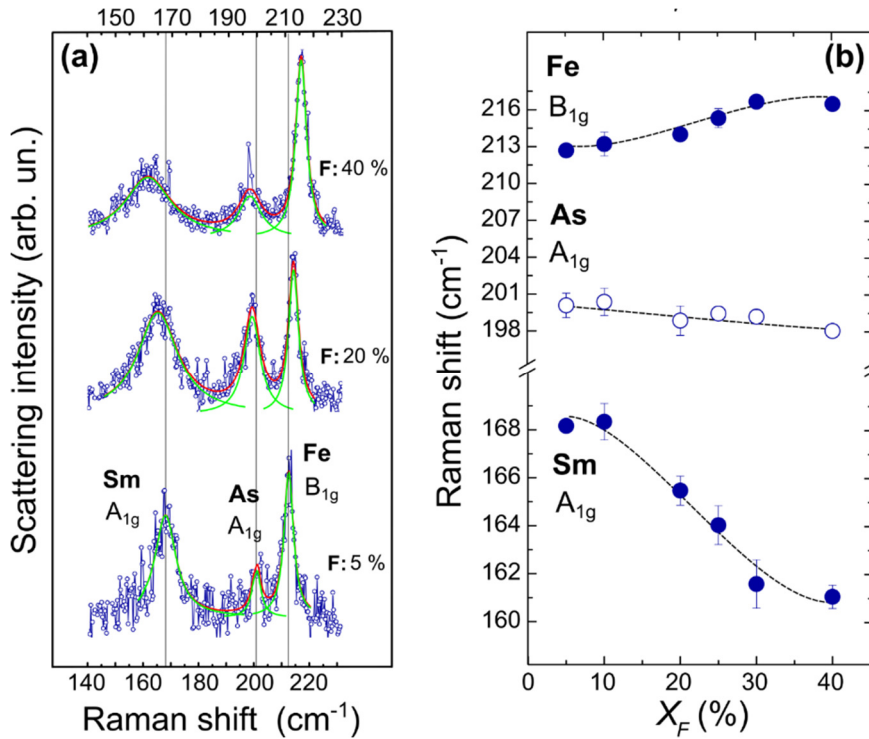


**Figure 4:** Temperature dependence of electrical resistivity  $\rho(T)$  for  $\text{SmFeAsO}_{1-x}\text{F}_x$  bulks. Measurements were conducted for the sample  $x = 0.05, 0.10, 0.20, 0.25, 0.30$ , and  $0.40$ . Figures (a) and (b) show the  $\rho(T)$  behaviour over the full temperature range up to 300 K and within the low-temperature interval of 30-60 K, respectively. The extracted transport parameters are: (c) the onset superconducting transition temperature ( $T_c^{\text{onset}}$ ), (d) the transition width ( $\Delta T$ ), (e) the resistivity at 300 K ( $\rho_{300\text{K}}$ ), and (f) the residual resistance ratio ( $RRR = \rho_{300\text{K}} / \rho_{60\text{K}}$ ) as a function of fluorine concentration ( $x$ ) for these  $\text{SmFeAsO}_{1-x}\text{F}_x$  bulks.

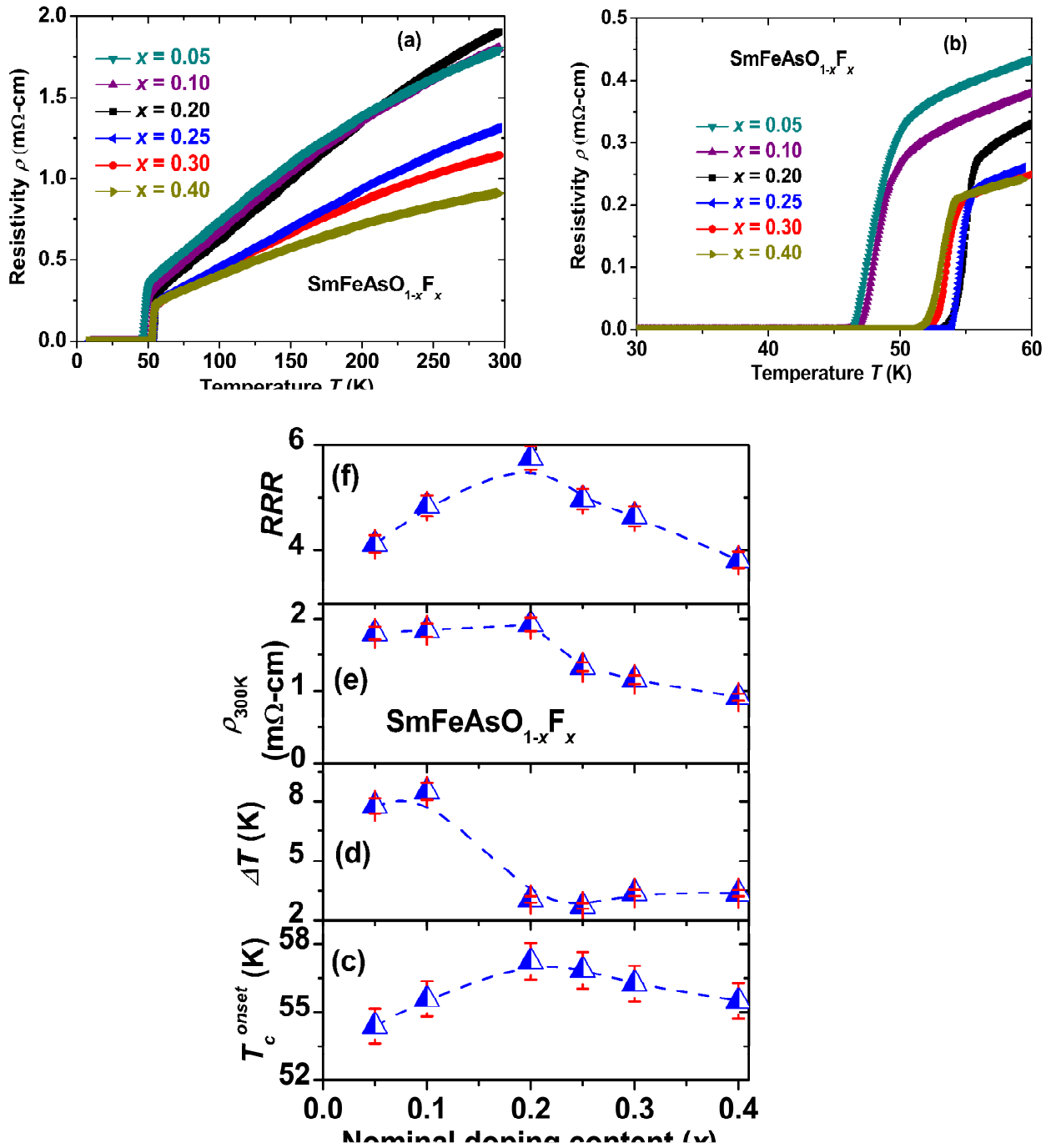


**Figure 5:** The field-dependent resistivity of  $\text{SmFeAsO}_{1-x}\text{F}_x$  bulks for the sample (a)  $x = 0.05$ , (b)  $x = 0.25$ , and (c)  $x = 0.40$  measured under the magnetic field of 0-9 T in the temperature range 20-70 K. The inset of each figure (a), (b) and (c) show the corresponding  $H$ - $T$  phase diagrams, where diamond symbols represent the upper critical field  $H_{c2}$  (determined at 90% of the normal-state resistivity  $\rho_n$ ) and triangle symbols denote the irreversibility field  $H_{irr}$  (determined at 10% of  $\rho_n$ ). Linear fits near  $T_c$  yield slopes  $dH_{c2}/dT|_{T=T_c} \approx -17.3, -5.7, -3.2 \text{ T K}^{-1}$  for  $x = 0.05, 0.25$ , and  $0.40$ , respectively.

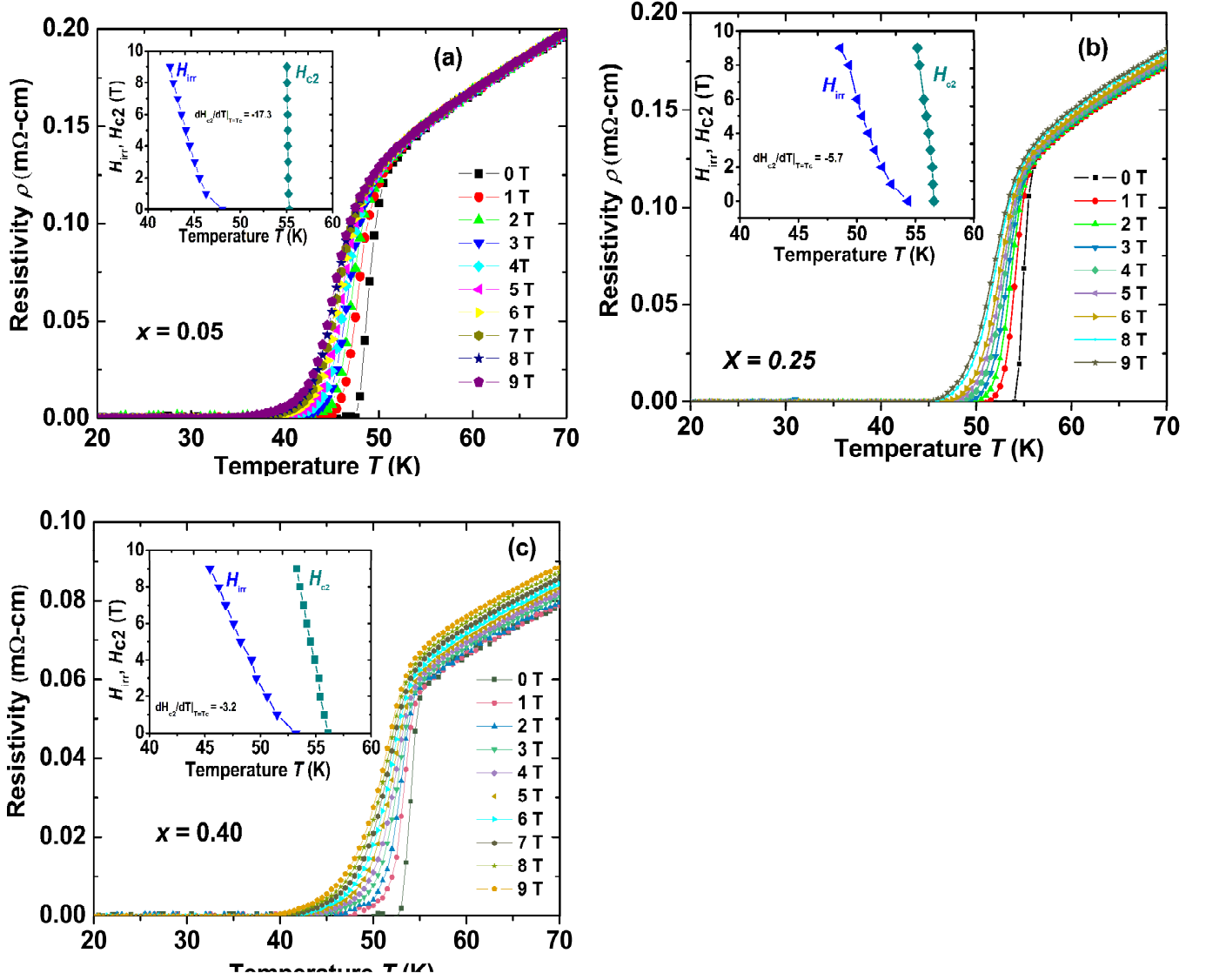


**Figure 6.** (a-c) Arrhenius plots of the normalized resistivity,  $(\rho/\rho_n)$  versus  $1/T$  for  $\text{SmFeAsO}_{1-x}\text{F}_x$  samples with  $x = 0.05, 0.25$ , and  $0.40$  measured under the magnetic field  $\mu_0 H = 0$  to  $9$  T. Here the resistivity is normalized by the normal state resistivity  $\rho_n$  just above the superconducting transition. The dashed red line in Figures (a)-(c) guides to show the linear fitting used to extract the activation energy ( $U_0/k_B$ ). (d) The magnetic field dependence of the extracted activation energy  $U_0/k_B$  is presented for the underdoped sample  $x = 0.05$ , optimal doped sample  $x = 0.25$  and the overdoped sample  $x = 0.40$ .

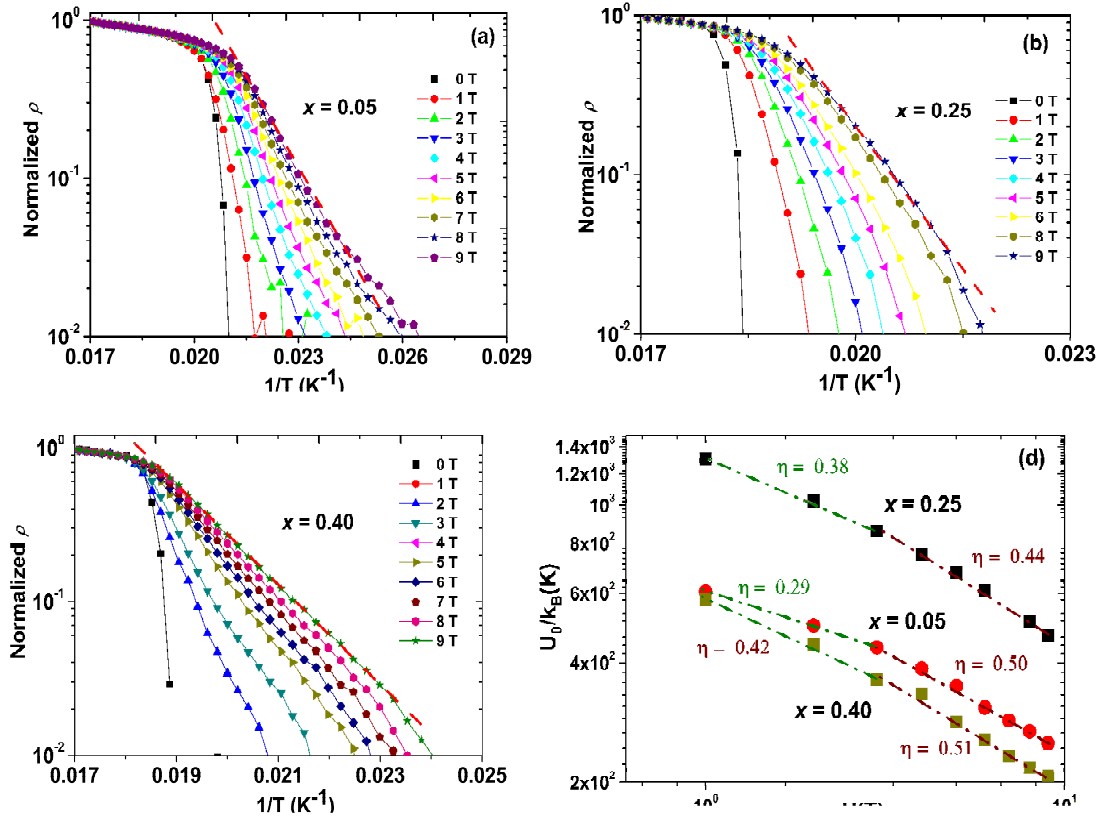


**Figure 7:** Magnetic properties of bulk  $\text{SmFeAsO}_{1-x}\text{F}_x$  bulks. **(a)** Temperature dependence of the normalized magnetic moment ( $M/M_{5K}$ ) recorded under zero-field-cooled (ZFC) and field-cooled (FC) conditions in an applied magnetic field of 20 Oe. **(b)** Variation of the critical current density ( $J_c$ ) at 5 K as a function of the applied magnetic fields. The inset in Figure (b) shows the field dependence of the pinning force ( $F_p$ ) at 5 K for the samples  $x = 0.05, 0.25$ , and  $0.40$ .

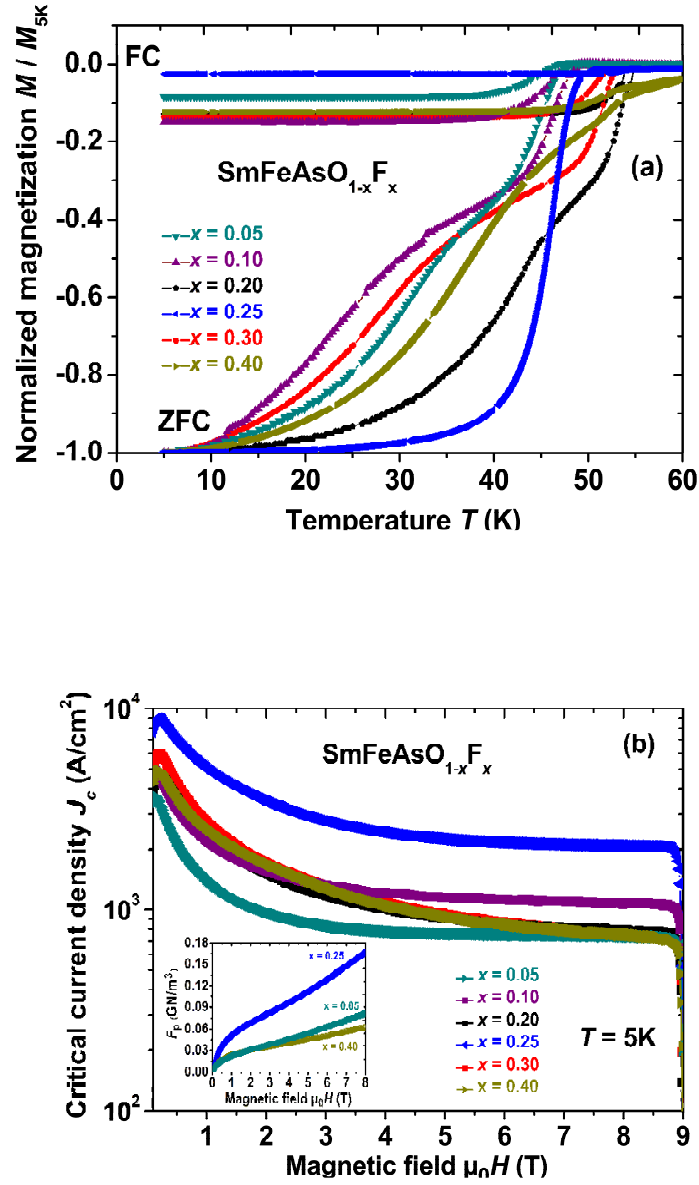


**Figure 8.** (a) Superconducting onset transition temperature  $T_c$  from resistivity measurements and (b) critical current density ( $J_c$ ) from magnetization measurements of  $\text{SmFeAsO}_{1-x}\text{F}_x$  samples prepared by the CA-HP process are plotted as a function of nominal fluorine content ( $x$ ). Three colour regions are used to depict the underdoped, optimal (Opt.) and overdoped regions. For comparison, black hexagons denote the transport onset  $T_c$  and  $J_c$  (from magnetization) of  $\text{SmFeAsO}_{1-x}\text{F}_x$  samples prepared by the low-temperature CSP method [6], while triangles correspond to  $\text{Sm1111}$  samples prepared by the high-temperature CSP method [23]. Error bars for our CA-HP processed samples are included in Figures (a) and (b).

